(Received 18 November 2025, Accepted 16 December 2025, Scheduled 13 January 2026)

Electromagnetic Performances Comparison of Partitioned Stator Flux Modulation Machines with Different Auxiliary Rotor Structures

Yifei Hu[1], Meimei Xu[1], Zhijian Ling[1,*], Wenxiang Zhao[1,2], and Zhaowei Wang[1]

[1]*School of Electrical and Information Engineering, Jiangsu University, Zhenjiang 212013, China*
[2]*School of Electric Power Engineering, Nanjing Institute of Technology, Nanjing 211167, China*

ABSTRACT: In this paper, the electromagnetic performances of partitioned stator flux modulation (PSFM) machines with different rotor structures are compared to highlight the advantages of the auxiliary rotor structures. Two novel auxiliary rotors are proposed to suppress electromagnetic vibration in PSFM machine. First, the PSFM machine topology and the analytical models for the outer air-gap permeance of the different rotors are introduced. Furthermore, a comparative analysis of the electromagnetic and vibrational performance between the different auxiliary rotor machines and the conventional rotor machine are conducted to validate the advantages of the proposed designs. Finally, machines with different auxiliary rotors are mounted onto the experimental platform for testing to validate the effectiveness of the theoretical analysis.

1. INTRODUCTION

In recent years, there has been growing interest in field-modulated permanent magnet (PM) machines based on the magnetic gear effect [1–3]. Compared to traditional permanent magnet synchronous machines, field-modulated PM machines offer high torque density and a highly sinusoidal back-EMF [4, 5]. A key characteristic of the field-modulated PM machines is its high torque output at low rotational speeds [6], making them well-suited for applications such as electric vehicles, heavy machinery, and wind power generation [7, 8].

Based on the installation location of the PMs, field-modulated PM machines can be classified into stator-PM machines and rotor-PM machines [9]. In rotor-PM machines, where the PMs are mounted on the rotor, issues such as poor heat dissipation and the risk of magnet detachment can arise under high-speed operation. These issues are effectively mitigated in stator-PM machine designs. In stator-PM field-modulated machines, however, both the PMs and the windings are located on the stator. This configuration leads to competition for the limited available space, imposing limitations on further improvements in torque density and electrical loading [10–12]. Consequently, a novel partitioned-stator flux-modulated (PSFM) machine topology has been proposed [13]. In the PSFM machine, the single stator in the stator-PM machine is partitioned into an inner stator and an outer stator. The PMs and the armature windings are located on the inner and outer stators, respectively. This novel configuration effectively addresses the issue of competition for limited stator space between PMs and armature windings, thereby enhancing the machine's torque density [14].

In field-modulated PM machine, the field modulation effect generates abundant flux density harmonics in the air gap of machine. These harmonics interact to produce numerous low-order radial force harmonics [15], which amplifies the electromagnetic vibration of the machine [16].

Numerous methods have been proposed to suppress electromagnetic vibration in field-modulated PM machine. In [17], an unequal stator modulated tooth structure was proposed to reduce electromagnetic vibration in field-modulated machines. In [18, 19], the authors introduced auxiliary slots at various rotor positions to suppress electromagnetic vibration in a field-modulated machine. In [20], skewed rotor/skewed stator structure was proposed to reduce electromagnetic vibration of field-modulated machine. In [21, 22], a novel rotor permanent magnet arrangement and an asymmetric stator tooth structure are proposed to modify the amplitude and phase of specific magnetic flux density harmonics for suppressing electromagnetic vibration. In [23, 24], a multi-physics analysis method is employed to investigate the effects of radial force modulation and dynamic eccentricity effect in the PM vernier machines. This study adopts the same multi-physics analysis method.

How to maintain or even enhance electromagnetic performance (such as torque) while suppressing electromagnetic vibration has emerged as a critical challenge in the field of field-modulated machines.

In this paper, two novel rotor structures are proposed to suppress electromagnetic vibration in a PSFM machine. The electromagnetic and vibration performance of PSFM machines with different rotor structures were compared. The proposed internal auxiliary slots rotor demonstrates a dual capability to suppress machine electromagnetic vibrations and enhance torque

* Corresponding author: Zhijian Ling (lzj1991@ujs.edu.cn).

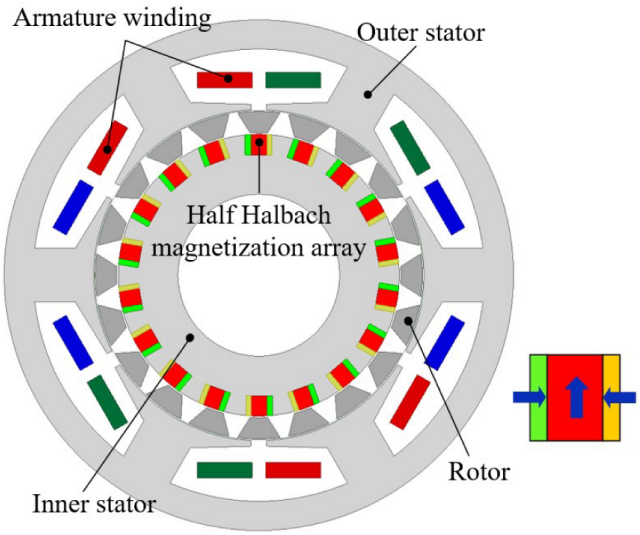

FIGURE 1. Topology of PSFM machine.

TABLE 1. Main parameters of PSFM machine.

Items	Value
Outer stator outer diameter (mm)	145
Outer stator inner diameter (mm)	94
Outer air-gap length (mm)	0.5
Inner air-gap length (mm)	0.5
Inner stator outer diameter (mm)	80
Inner stator inner diameter (mm)	46
Axial length (mm)	60
Rated speed (r/min)	660
Rated current (A)	7
Turns per coil	66
PM material	NdFe35
Iron lamination	DW315-50
Rated power	1 kW
Rated voltage	380 V
Rated torque	15 Nm

output. The proposed internal auxiliary slots rotor demonstrates superior performance in suppressing electromagnetic vibration in the machine. First, the PSFM machine topology and different rotor structure topologies, rotor optimization process along with the air gap permeance models of different rotor machines, are introduced in Section 2. Section 3 presents a comparative analysis of the electromagnetic and vibrational performance between the two novel-rotor machines and the conventional rotor machine, to demonstrate the advantages of the proposed rotors. In Section 4, prototype machines employing different rotor topologies were fabricated and tested on an experimental platform to validate the theoretical analysis.

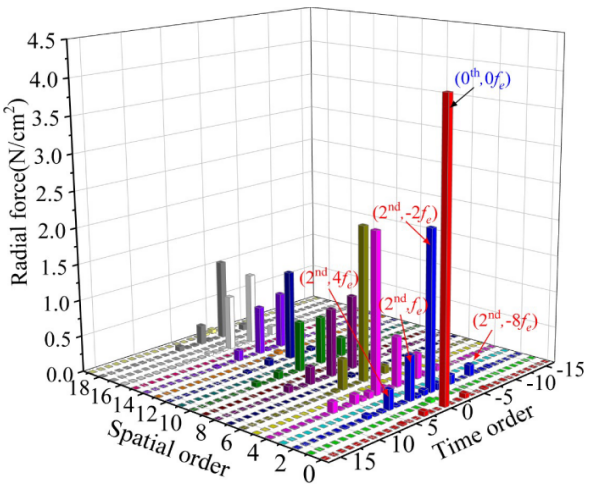

FIGURE 2. 2-D radial force spectrums of PSFM machines.

2. MACHINE TOPOLOGY AND NOVEL ROTOR TOPOLOGY

2.1. Topology of PSFM Machine

The 2D model of the PSFM machine studied in this paper is shown in Fig. 1. According to the magnetic field modulation theory, the number of pole pairs of PMs P_{pm}, the number of rotor iron pieces N_r, and the equivalent pole pairs of outer stator armature windings P_{arm}, must meet the following relationship:

$$P_{pm} = N_r - P_{arm} \tag{1}$$

In the PSFM machine, the inner stator is equipped with an 18-pair pole Halbach magnetization array, which can reduce magnetic leakage in the PSFM machine. The outer stator houses a 6-slot/2-pole-pair concentrated winding, while the rotor consists of 20-pole-pair flux-modulating iron pieces. The rotor iron pieces, which are linked by non-magnetic materials, modulate the PM and armature magnetic fields to produce the working harmonic essential for a normal machine operation. The main structural design parameters of the PSFM machine are shown in Table 1.

2.2. Radial Force and New Rotor Topology

The expression for the radial electromagnetic force in the PSFM machine's outer air gap can be expressed as:

$$Fr\left(\theta,t\right) = \frac{b_r^2\left(\theta,t\right)}{2\mu 0} \tag{2}$$

where $b_r(\theta,t)$ is the radial air-gap flux density. A 2D-FFT was performed on the 3D waveform of the radial electromagnetic force in the outer air gap of the PSFM machine, yielding the spatial and temporal order distribution diagrams, as shown in Fig. 2. The relationship between the vibration amplitude of a machine and the radial force harmonics can be expressed as:

$$D_s \propto \frac{F}{\left(M_1^2-1\right)^2} \cdot \frac{1}{1-\left(\frac{f}{f_c}\right)^2} \tag{3}$$

TABLE 2. The sensitivity values of rotor-auxiliary slot structural parameters.

	Average torque (Nm)		Torque ripple (%)		2nd-radial force (N/cm^2)	
	Surface	Internal	Surface	Internal	Surface	Internal
θ_1	0.11	0.10	−0.32	0.14	0.21	0.24
β	0.15	0.18	−0.08	−0.12	0.17	0.27
H_1	−0.13	−0.42	0.29	0.22	−0.34	−0.39
H_2	-	0.23	-	-0.09	-	0.18

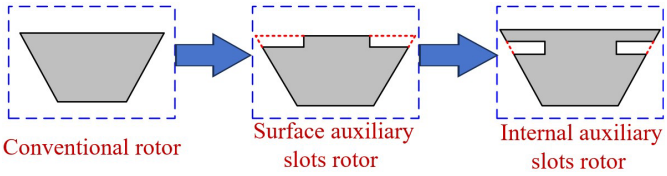

FIGURE 3. Topology structure of the proposed rotor.

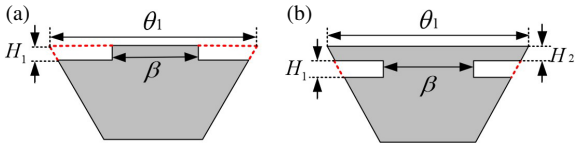

FIGURE 4. The selection of rotor design variables in the multi-objective optimization. (a) Surface slots rotor. (b) Internal slots rotor.

where D_s is the stator system deformation; F, M_1 denote the electromagnetic force harmonic amplitude and order, respectively; f and f_c denote the electromagnetic force harmonic frequency and machine natural frequency. From Eq. (3), it can be seen that D_s is directly proportional to F and approximately inversely proportional to the fourth power of M_1. Thus, radial forces with low spatial orders contribute more significantly to electromagnetic vibration than those with high spatial orders. Since the 0th radial force has a fundamental frequency of 0 Hz, which has no effect on electromagnetic vibration, the 2nd radial force is identified as the dominant contributor to the electromagnetic vibration. As shown in Fig. 2, the primary frequencies of the 2nd radial force are f_e, $2f_e$, $4f_e$, and $8f_e$ Hz. (The fundamental frequency of PSFM machines is $f_e = N_r\omega_r/60$, and ω_r is the mechanical speed of rotor rotation.)

As shown in Fig. 3, two novel rotor topologies are proposed to suppress machine electromagnetic vibrations. However, these new rotor structures produce a non-negligible impact on the electromagnetic performance of the PSFM machines. Multi-objective optimization strategy based on the particle swarm algorithm was employed to determine the optimal structural parameters of the novel rotor. The selection of optimized design parameters is shown in Fig. 4. The calculated parameter-sensitivity results for the proposed surface auxiliary slots rotor and internal auxiliary slots rotor are summarized in Table 2. Through the optimization of the rotor-auxiliary slot structure, the amplitude of the 2nd-radial force causing the dominant vibration was minimized, while the average torque was maximized, and the torque ripple was minimized. The optimization results of the novel rotor are presented in Table 3.

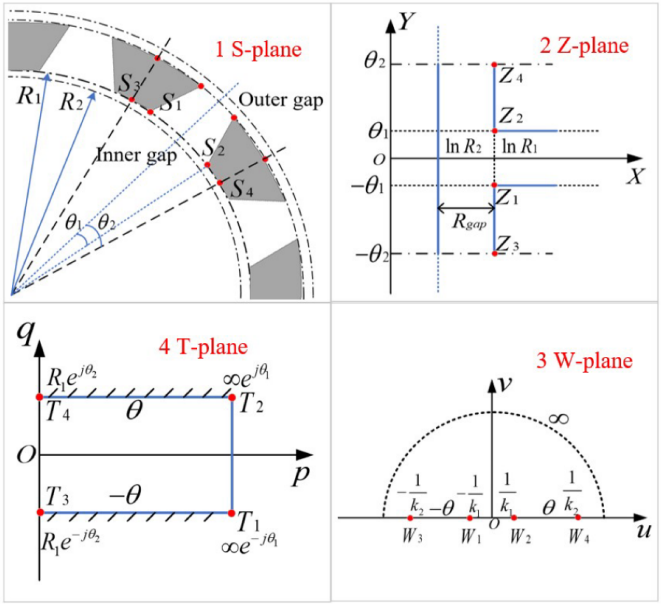

FIGURE 5. Complete flowchart of conformal mapping method.

2.3. Air-Gap Permeance Model

The introduction of auxiliary slots changes the outer air-gap permeance distribution, so establishing outer air gap permeance models for the different rotor structures is necessary.

For the double air-gap PSFM machine, the traditional permeability calculation method may have a large error, so the conformal mapping method is used to accurately derive the air-gap permeance models. Considering the symmetry of the rotor modulating blocks' structure of PSFM machine, a region within one pole pitch is selected as the minimum analytical modeling region. By applying a logarithmic transformation, the modeling region in the S-plane is first mapped into the Z-plane. Subsequently, key geometric points in the Z-plane are transformed into the W-plane, and finally into the T-plane. The coordinates of the principal geometric points within the W-plane and T-plane are illustrated in the Fig. 5. By taking the gradient of the scalar magnetic potential Ω in the T-plane, the magnetic flux density at any point in the S-plane is obtained as:

$$B_{slot} = \mu_0 \frac{\partial t}{\partial s} = \mu_0 \frac{\partial t}{\partial w}\frac{\partial w}{\partial z}\frac{\partial z}{\partial s}$$

$$= \mu_0 \frac{\pi}{r\alpha_2}\frac{\Omega_0}{K(k_1^2)}\frac{cn\alpha}{sn\alpha * dn\alpha}\sqrt{\frac{1-k_1^2w^2}{1-k^2w^2}} \quad (4)$$

TABLE 3. Design variables and electromagnetic performance of the machine before and after optimization.

Parameter	Surface auxiliary solts rotor		Internal auxiliary solts rotor	
	Initial	optimized	Initial	optimized
θ_1	15	15.2	15	15.3
β	0.5	0.48	0.5	0.52
H_1	0.7	0.51	1	1.12
H_2	-	-	1	0.91
Average torque (Nm)	13.97	14.19	15.12	15.43
Torque ripple (%)	18.8%	16.9%	15.2%	15.3%
2nd-radial force (N/cm^2)	1.5627	1.5154	1.8376	1.7223

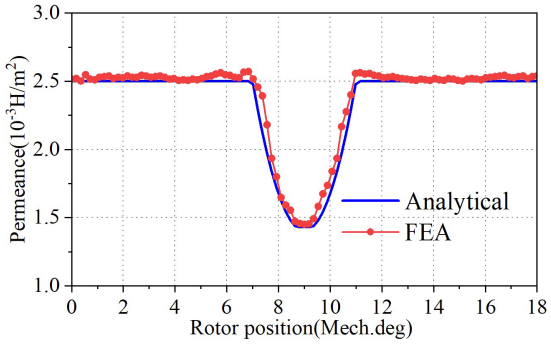

FIGURE 6. FEA and analytical results of permeance models within one pole pitch.

When the machine rotor is slotless, the magnetic flux density at any point in the S-plane is expressed as:

$$B_{slotless} = \mu_0 \frac{\Omega_0}{r \ln(R_1/R_2)} \tag{5}$$

According to Eqs. (4) and (5), the air-gap permeance of the PSFM machine can be expressed as:

$$\begin{aligned} \Lambda =& \frac{B_{slot}}{B_{slotless}} \\ =& \frac{\pi \ln(R_1/R_2)\, cn\left(\varphi/k^2\right)}{\alpha_2 K\left(k_1^2\right) sn\left(\varphi/k^2\right) * dn\left(\varphi/k^2\right)} \sqrt{\frac{1-k_1^2 w^2}{1-k^2 w^2}} \\ h(w) =& \frac{\pi}{\alpha_2}\left(\ln\frac{r}{R_2} + j\alpha\right) + \prod\left(p, \varphi/k^2\right) \\ & - p\frac{sn\left(\varphi/k^2\right) * dn\left(\varphi/k^2\right)}{cn\left(\varphi/k^2\right)} = 0 \end{aligned} \tag{6}$$

The projection flow of the conformal mapping method is shown in Fig. 5. The permeance models within one pole pitch derived from the analytical method and the FEA method are presented in Fig. 6. The relative error between the permeance models obtained from the analytical method and FEA method is small.

The air-gap permeance model for the conventional rotor PSFM machine can be derived using the conformal mapping method, as shown in Fig. 7(a). Building on the conformal mapping method, accounting for the structural parameters and position of the auxiliary slots, as well as the B-H curve of the rotor material, the air-gap permeance models for the two novel rotor machines can be derived, as shown in Figs. 7(b) and 7(c). The air-gap permeance models for the different rotor structures were subjected to Fourier expansion. The harmonic components of permeance waveform of the PSFM machine are illustrated in Fig. 8.

3. PERFORMANCE COMPARISON OF PSFM MACHINES WITH DIFFERENT ROTORS

3.1. Comparison of Electromagnetic Performance

To validate the advantages of the proposed novel-rotor PSFM machines, the electromagnetic performance of different rotor machines was compared at rated current and rated speed.

The no-load back-EMF waveforms of PSFM machines with different rotor structures are shown in Fig. 9. As shown in the Fig. 9(a), the no-load back-EMF waveform of the surface auxiliary slots PSFM machine exhibits a reduction in amplitude. The no-load back-EMF harmonics of PSFM machines with different rotor structures are shown in Fig. 9(b). The fundamental amplitude of the no-load back-EMF in the surface auxiliary slots PSFM machine is 94.2 V, which is 6.8% lower than that of the conventional rotor machine. The fundamental amplitude of the no-load back-EMF in the internal auxiliary slots PSFM machine is 103.2 V, which is 2.2% higher than that of the conventional rotor machine. By relocating the auxiliary slots beneath the rotor upper surface, the internal auxiliary slots PSFM machine achieves a higher fundamental amplitude of the no-load back-EMF.

The novel rotor structure significantly changes both the radial and tangential flux density components in the outer air-gap. Fig. 10 illustrates the outer air-gap radial flux density in the PSFM machines with different rotor structures when operated on load. As shown in Fig. 10(b), the newly proposed rotor structure effectively suppresses the amplitudes of the 2nd, 4th, 8th, 10th, 14th, 16th, 18th flux density harmonics.

As shown in Fig. 11. for rotor with internal auxiliary slots, the direction of the line of magnetic flux passing above the

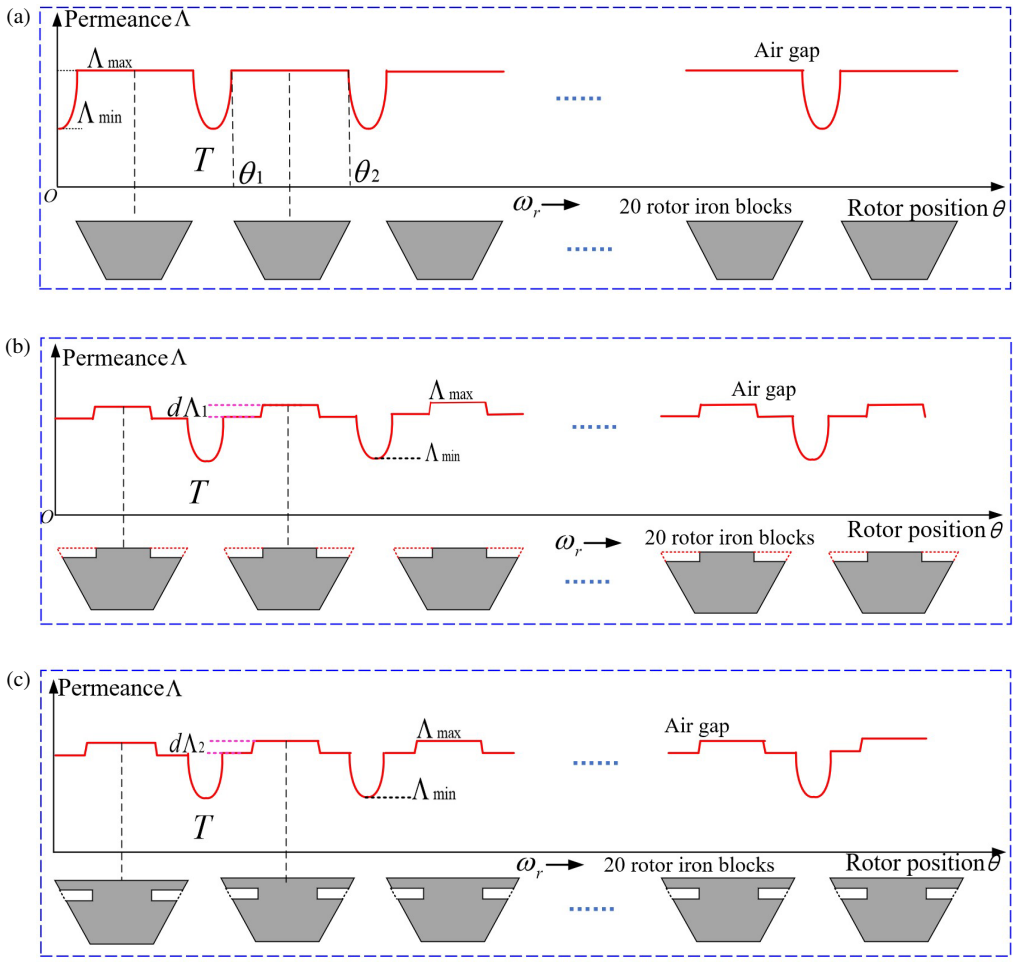

FIGURE 7. Outer air-gap permeance model of PSFM machine with different rotor.

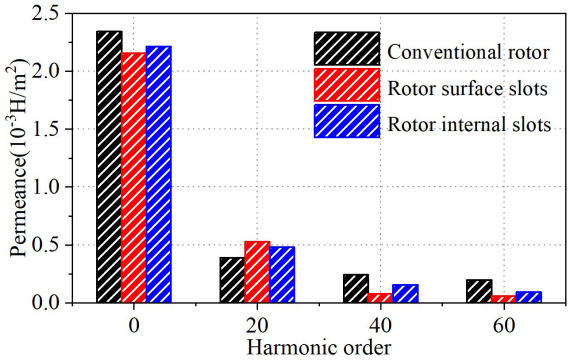

FIGURE 8. Harmonic components of outer air-gap permeance model.

auxiliary slots is changed due to the presence of the auxiliary slots, the direction of the magnetic flux density within the outer air-gap changes, thus the flux density tangential component increases. Fig. 12 illustrates the outer air-gap tangential flux density in the PSFM machines with different rotor structures when operated on load. As shown in Figs. 12(a) and 12(b), the amplitude of the tangential flux density increases in the outer air gap of the machine with internal auxiliary slots rotor.

The output torque waveforms of PSFM machines with different rotors are shown in Fig. 13. For the surface auxiliary slots

TABLE 4. Torque generated by working harmonics.

	Inner gap generates (Nm)		Outer gap generates (Nm)	
	2nd	18th	2nd	18th
Conventional rotor	0.89	12.68	1.48	0.088
Rotor surface slots	0.83	12.17	1.12	0.072
Rotor internal slots	0.90	12.64	1.84	0.108

rotor machine, the introduction of the auxiliary slots increases the air-gap reluctance, resulting in a decrease in the average torque. However, the internal auxiliary slot rotor structure effectively enhances the average torque of the PSFM machine.

According to the flux-modulation principle, the electromagnetic torque of the PSFM machine is generated by the interaction of the 2nd and 18th operating harmonics of the magnetic fields in the inner and outer air gap. The electromagnetic torque generated by the PSFM machine can be expressed as follows:

$$T_{sum}(t) = \frac{r^2 l}{\mu 0} \int_0^{2\pi} B_r B_t d\theta = \sum_k T_k(t) \tag{7}$$

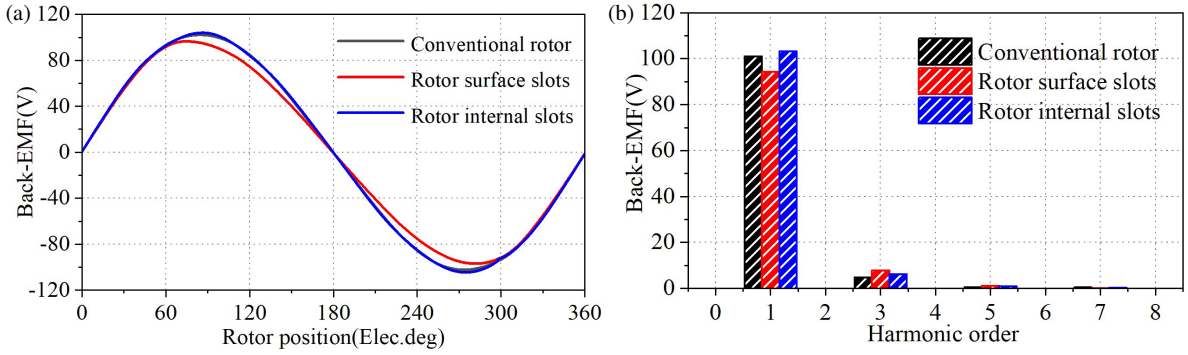

FIGURE 9. Comparison of no-load back-EMF of PSFM machines with different rotor types. (a) Waveforms. (b) Harmonic components.

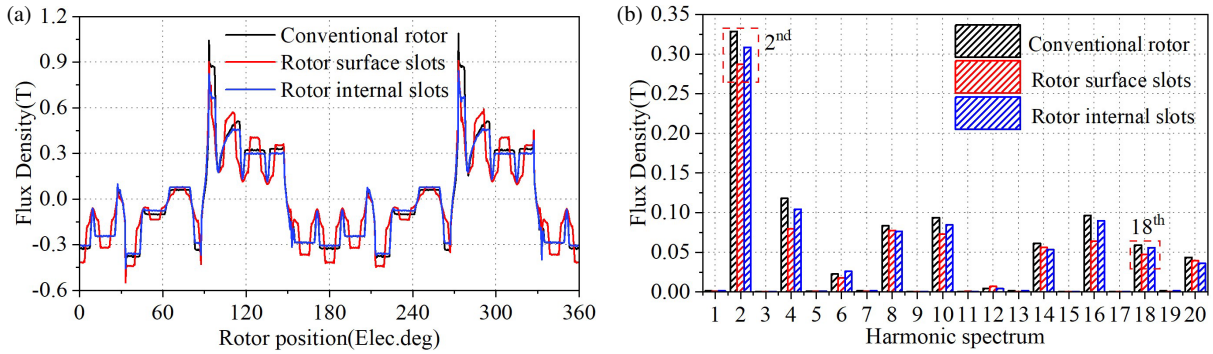

FIGURE 10. Comparison of outer air-gap radial flux density of both PSFM machines on load. (a) Waveforms. (b) Harmonic components.

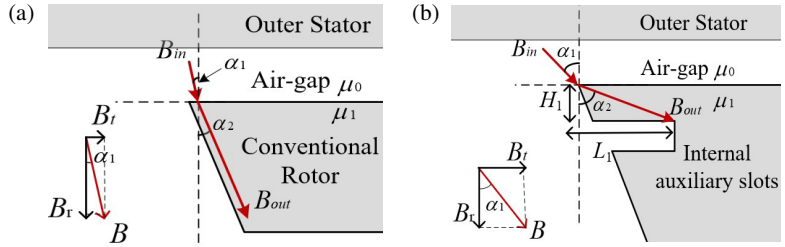

FIGURE 11. Direction of line of magnetic flux with different rotor. (a) Conventional rotor. (b) Internal auxiliary slots rotor.

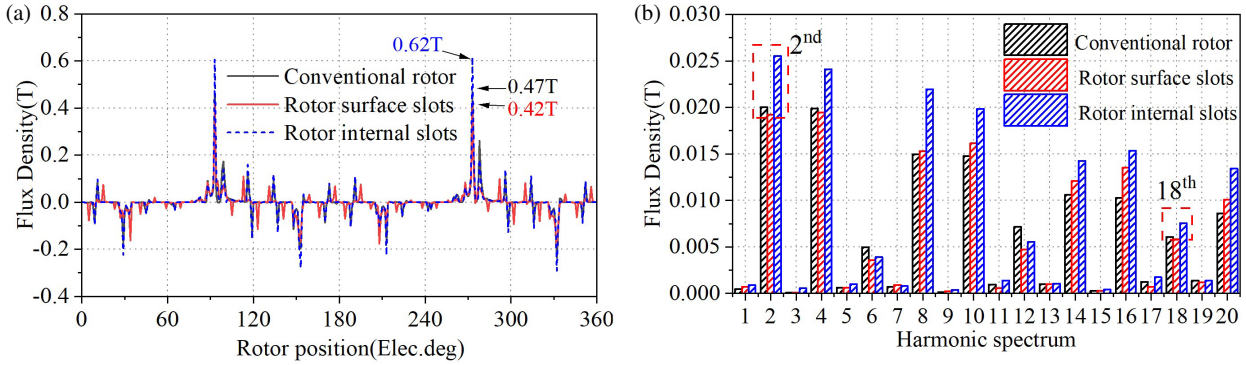

FIGURE 12. Comparison of the outer air-gap tangential flux density of both PSFM machines on load. (a) Waveforms. (b) Harmonic components.

$$T_k(t) = \frac{\pi r^2 l}{\mu_0} B_{rk} B_{tk} \cos\left[\theta_{rk}(t) - \theta_{tk}(t)\right] \quad (8)$$

where r is the radius of air gap, l is the axial length of the machine, B_r and B_t are the radial and tangential air gap flux density of the machine air gap. B_{rk} is the radial flux density amplitude of the kth harmonic, B_{tk} is the tangential flux density amplitude of the kth harmonic, θ_{rk} is the radial flux density phase angle of the kth harmonic, θ_{tk} is the tangential flux density phase angle of the kth harmonic. The flux density har-

TABLE 5. Comparison of other electromagnetic performance of PSFM machines with different rotor structures.

	Conventional rotor machine	Rotor surface slots machine	Rotor internal slots machine
Torque ripple (%)	11.4	16.8	15.3
Cogging Torque (Nm)	0.23	0.6	0.26
Iron loss (W)	45.9	38.7	42.4
PM eddy current loss (W)	0.89	0.82	0.83
Copper loss (W)	92.5	92.5	92.5
Efficiency (%)	88.2	88.1	88.7
Power factor	0.66	0.62	0.65

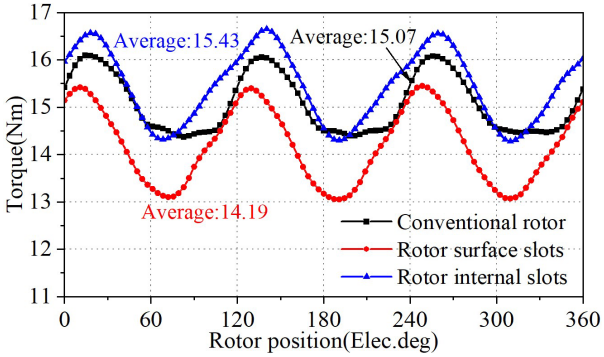

FIGURE 13. Torque waveforms of PSFM machines with different rotor types.

TABLE 6. Modal analysis of stator assembly.

Modal order	2	3	4
Modal shape	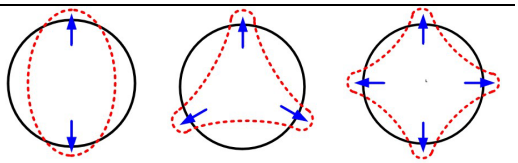		
Nature frequency	1572Hz	2922Hz	4556Hz

monics contribution to the torque from the inner/outer air gap of the PSFM is calculated based on Eq. (7) and Eq. (8), as illustrated in Table 4. As illustrated in the Fig. 7(b), the introduction of auxiliary slots in the surface auxiliary slot rotor machine increases the air-gap reluctance. This increase leads to a reduction in the amplitudes of the 2nd and 18th working harmonics, consequently suppressing the torque contribution from these harmonics. As shown in Fig. 12(b), the internal auxiliary slot rotor structure enhances the tangential components of the 2nd and 18th working harmonics, thereby increasing the torque contributed by these harmonics.

The other electromagnetic performance of PSFM machines with different rotor topologies is presented in Table 5. Based on Table 5, the machine with surface/internal auxiliary slots rotor demonstrates a noticeable suppression of core losses, machines with different rotor structures exhibit little difference in efficiency and power factor. The introduction of rotor auxiliary slots, which increases both the cogging torque and the back-EMF total harmonic distortion (THD), consequently increases the fluctuation rate of the PSFM machine's load torque.

Under extreme operating conditions — such as temperatures exceeding 150°C, strong reverse magnetic fields (short-circuit current $>$ 300% rated value), and severe mechanical shock ($>$ 10 G) — permanent magnets can undergo demagnetization, resulting in a loss of magnetic flux density. This, in turn, leads to a decline in electromagnetic performance, including torque density and efficiency. Severe mechanical shocks or prolonged overload conditions can cause damage to the PSFM machine's mechanical structure.

3.2. Comparison of Electromagnetic Vibration Performance

According to machine vibration theory, the interaction of flux density harmonics within the air gap generates radial force harmonics. These radial force harmonics cause electromagnetic vibration in the machine. Therefore, it is concluded that suppressing the amplitudes of low-order radial force harmonics effectively suppresses electromagnetic vibration in the machine.

The comparison of the radial force waveforms and harmonics in the outer air gap for PSFM machines with different rotors is shown in Fig. 14. New rotor structure reduces the amplitude of the 0th permeance harmonics to reduce the amplitude of flux density harmonics like 2nd, 4th, 8th, 10th, 14th, 16th, 18th…. These high-amplitude flux density harmonics interact to generate low-order radial force harmonics. Therefore, as illustrated in Fig. 14(b), the amplitude of low-order radial force harmonics (2nd, 4th) in the outer air gap of both new rotor structures machines is significantly reduced, which will effectively suppress electromagnetic vibration in the PSFM machine.

The vibration analysis for PSFM machines with different rotors was conducted using a Maxwell-Workbench co-simulation. First, the calculation of the radial electromagnetic force in the outer air gap was performed on the 2D machine model in Maxwell. Subsequently, a 3D structural model of the machine stator and housing system was constructed in Workbench. The materials were defined, and a modal analysis was conducted to calculate the mode shapes and natural frequencies of the stator and housing system. The mode shapes and natural frequencies of the stator and housing system are shown in Table 6. Finally, the calculated radial electromagnetic forces were imported and applied as concentrated forces on the stator teeth

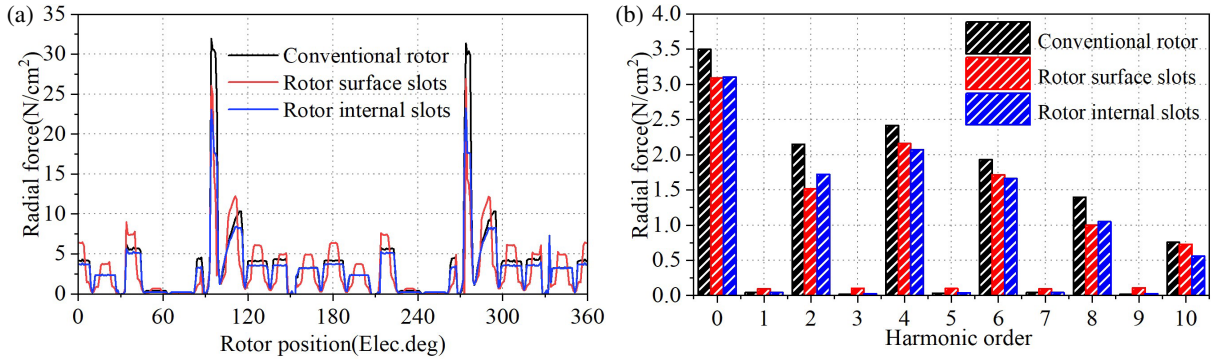

FIGURE 14. Comparison of outer air-gap radial force of PSFM machines on load. (a) Waveforms. (b) Harmonic components.

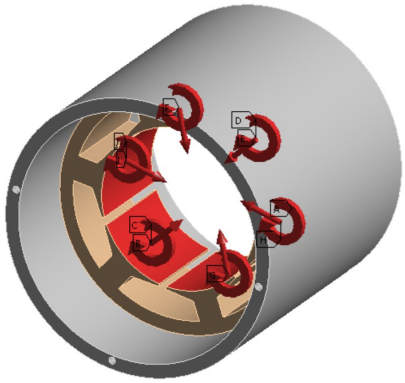

FIGURE 15. Equivalent diagram of electromagnetic forces at stator tooth surface.

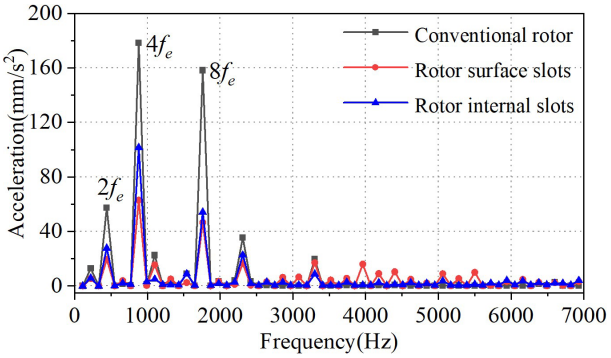

FIGURE 16. Comparison of vibration acceleration in PSFM machines with different rotor structures.

FIGURE 17. Stamping sheet for rotor. (a) Conventional rotor. (b) Surface auxiliary slots rotor. (c) Internal auxiliary slots rotor.

within the structural model, as illustrated in Fig. 15. The modal superposition method was employed to calculate the electromagnetic vibration of the PSFM machine. The surface vibration acceleration of the PSFM machines with different rotors is shown in Fig. 16. The peak vibration acceleration appears at $2f_e$, $4f_e$, $8f_e$ Hz, which is consistent with the frequency of radial force. As the amplitude of low-order radial force harmonics is reduced, the vibration acceleration amplitude of the newly proposed rotor machines shows a significant reduction, confirming the effectiveness of two proposed rotor structures in suppressing PSFM machine electromagnetic vibration.

4. EXPERIMENTAL VERIFICATION

To validate the theoretical analysis, rotors with different structures were fabricated and assembled into the PSFM prototype. Rotor stamping sheet with different structures is shown in Fig. 17. A complete PSFM machine rotor is composed of numerous stamping sheets combined with non-magnetic materials. Fig. 18 shows the outer stator, inner stator, permanent magnets, and the fully assembled rotor of the PSFM machine. The PSFM machines with different rotor structures were installed on the test platform for testing. The experimental platform and prototype are shown in Fig. 19.

A torque sensor (model: DYN) was employed, with a sensitivity of 0.1%. F.S, and a sampling frequency of 1000 Hz. A vibration acceleration sensor (model: SSF310AT) was used, with a sensitivity of 100 mV/g and a sampling frequency of 1024 Hz. An acceleration sensor was mounted at the mid-point of the machine housing surface.

With the machine operating at 660 rpm and $i = 7$ A, the torque waveforms of the machines with different rotors, as measured by a torque sensor, are presented in Fig. 20. The measured average output torque of the PSFM machine shows good agreement with the FEA results. The torque measurement results in-

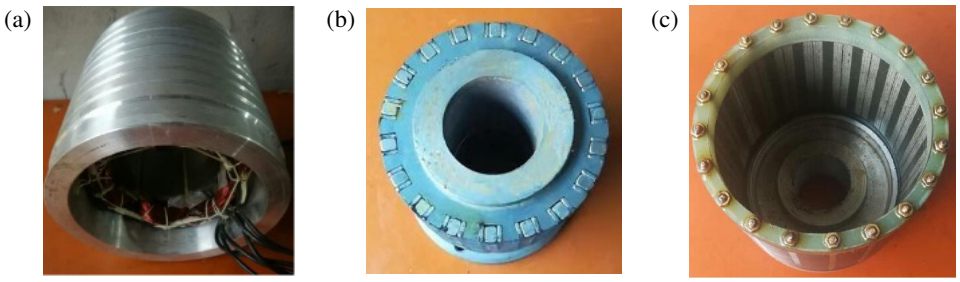

FIGURE 18. Structure of stator and rotor in prototype. (a) Outer stator. (b) Inner stator and PMs. (c) Rotor.

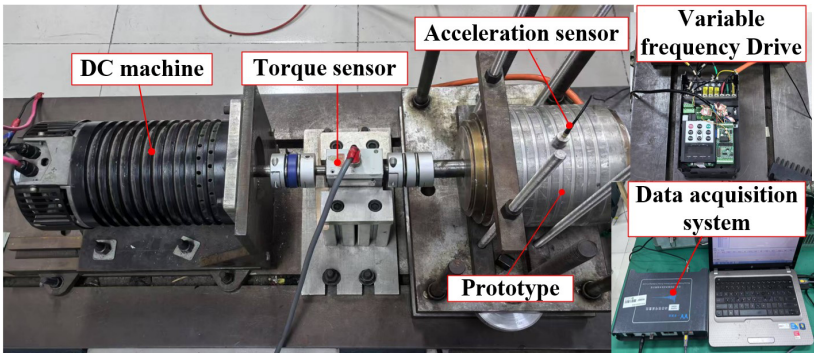

FIGURE 19. Prototype and experimental platform.

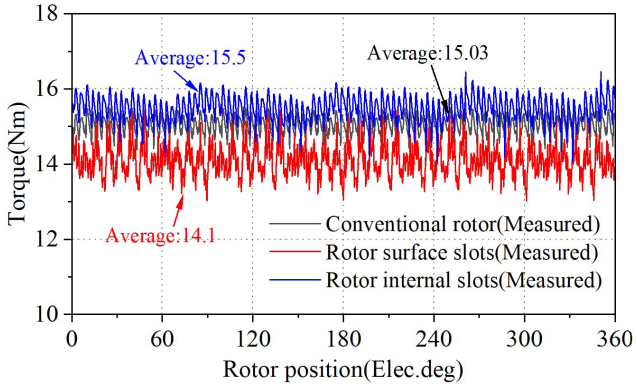

FIGURE 20. The PSFM machine torque waveform measured by torque sensor.

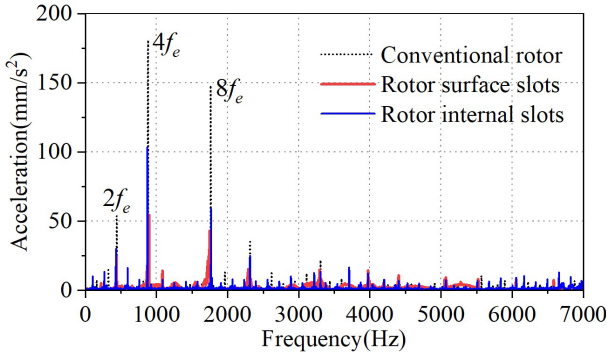

FIGURE 21. The PSFM machine vibration acceleration measured by acceleration sensor.

TABLE 7. Comparison of measured and FEA results.

	Average torque (Nm)	Torque ripple (%)	Peak vibration acceleration (mm/s^2)		
			$2f_e$	$4f_e$	$8f_e$
Measured result	15.03	11.4%	53.6	181.2	148.3
FEA result	15.07	12.2%	57.5	178.4	158.2
Error	2.7%	7%	7.3%	1.6%	6.7%

dicate that the proposed internal auxiliary slots rotor enhances the PSFM machine's output torque, while the surface auxiliary slots rotor machine exhibits a reduction in torque, which is consistent with the theoretical analysis. The spectra of the surface vibration acceleration for the different rotor PSFM machines are shown in Fig. 21. The time-domain vibration acceleration signal acquired by the acceleration sensor was processed and converted into its frequency-domain representation, as shown in Fig. 21. The measured frequency and amplitude of the vibration acceleration peak are in agreement with the FEA results. The vibration acceleration measurements indicate that the vibration acceleration amplitudes at various frequencies show a

significant reduction in the two new rotor machines, demonstrating the effective suppression of electromagnetic vibration in the PSFM machine achieved by these proposed rotor structures.

The errors between the measured and FEA-derived results of torque and vibration acceleration for the conventional rotor PSFM machine are presented in Table 7. Several factors — including machining tolerances during prototype fabrication, friction between the rotor, shaft, and other components, and the mounting method of the prototype on the test platform — can introduce errors into the measured torque and vibration acceleration. In general, the discrepancies between the measurement results and the FEA predictions remain within an acceptable range.

5. CONCLUSION

In this paper, two novel PSFM machine rotor structures are proposed to suppress electromagnetic vibration in the machine. Surface auxiliary slots rotor yields a more effective reduction of electromagnetic vibration in the PSFM machine. The internal auxiliary slot rotor effectively suppresses machine electromagnetic vibration while increasing the average output torque of the PSFM machine by increasing the tangential component of the air gap flux density. The following conclusions are drawn from both software simulations and experimental results:

(1) In this study, by changing the outer air-gap permeance distribution, the two proposed novel rotor structures suppress the amplitudes of the specific flux density harmonics responsible for generating low-order radial force harmonics, thereby achieving effective mitigation of these radial force harmonics. Therefore, two proposed novel rotor structures effectively suppress electromagnetic vibration in PSFM machines.

(2) Compared with the conventional rotor machine and surface auxiliary slots rotor machine, internal auxiliary slot rotor machine exhibits higher fundamental values of no-load back-EMF and higher average torque. The internal auxiliary slot rotor structure effectively enhances the amplitude of the tangential component of the air gap flux density, which significantly improves the PSFM machine's electromagnetic performance.

Future work will investigate the impact of new stator, rotor, and permanent magnet topologies on the electromagnetic vibration characteristics of other Flux-modulation machines.

ACKNOWLEDGEMENT

This work was supported in part by the National Natural Science Foundation of China under Grant 52307057 and 52207056, in part by the National Natural Science Foundation of Jiangsu Province under Grant BK20230539, and in part by the Key Research and Development of Zhenjiang under Grant GY2023011.

REFERENCES

[1] Chen, H., Z. Zhu, Z. Zhang, and H. Wang, "Comparative analysis of consequent-pole PM Vernier machines with different rotor types," *IEEE Transactions on Transportation Electrification*, Vol. 10, No. 1, 450–461, Mar. 2024.

[2] Xu, L., Z. Chen, W. Zhao, and T. Jiang, "Analysis of a fault-tolerant dual-permanent-magnet vernier machine with hybrid stator," *IEEE Transactions on Transportation Electrification*, Vol. 10, No. 3, 6559–6570, Sep. 2024.

[3] Bi, Y., W. Fu, S. Niu, X. Zhao, J. Huang, and Z. Qiao, "Torque enhancement of a dual-PM flux-switching machine with improved multiple high-order working harmonics," *IEEE Transactions on Transportation Electrification*, Vol. 10, No. 2, 2830–2843, Jun. 2024.

[4] Xu, L., W. Zhao, R. Li, and S. Niu, "Analysis of rotor losses in permanent magnet vernier machines," *IEEE Transactions on Industrial Electronics*, Vol. 69, No. 2, 1224–1234, Feb. 2022.

[5] Xiang, Z., Z. Lu, X. Zhu, M. Jiang, D. Fan, and L. Quan, "Research on magnetic coupling characteristic of a double rotor flux-switching PM machine from the perspective of air-gap harmonic groups," *IEEE Transactions on Industrial Electronics*, Vol. 69, No. 12, 12 551–12 563, Dec. 2022.

[6] Cao, L., Y. Zuo, X. Zhu, S. Xie, and C. H. T. Lee, "Investigation of permanent-magnet vernier machine with fractional-slot nonoverlapping windings for direct-drive application," *IEEE Transactions on Transportation Electrification*, Vol. 10, No. 2, 3383–3395, Jun. 2024.

[7] Liu, J., X. Li, B. Yan, W. Hua, and X. Wang, "Electromagnetic performance analysis of a field-modulated permanent magnet motor using improved hybrid subdomain method," *IEEE Transactions on Energy Conversion*, Vol. 38, No. 3, 1753–1766, Sep. 2023.

[8] Kim, J. H., Y. Li, and B. Sarlioglu, "Novel six-slot four-pole axial flux-switching permanent magnet machine for electric vehicle," *IEEE Transactions on Transportation Electrification*, Vol. 3, No. 1, 108–117, Mar. 2017.

[9] Cheng, M., W. Hua, J. Zhang, and W. Zhao, "Overview of stator-permanent magnet brushless machines," *IEEE Transactions on Industrial Electronics*, Vol. 58, No. 11, 5087–5101, Nov. 2011.

[10] McFarland, J. D., T. M. Jahns, and A. M. EL-Refaie, "Analysis of the torque production mechanism for flux-switching permanent-magnet machines," *IEEE Transactions on Industry Applications*, Vol. 51, No. 4, 3041–3049, Jul.–Aug. 2015.

[11] Zhang, H., W. Hua, M. Hu, D. Gerada, and C. Gerada, "The influence of winding location in flux-switching permanent-magnet machines," *IEEE Transactions on Magnetics*, Vol. 55, No. 7, 1–5, Jul. 2019.

[12] Shi, J. T., A. M. Wang, and Z. Q. Zhu, "Influence of PM- and armature winding-stator positions on electromagnetic performance of novel partitioned stator permanent magnet machines," *IEEE Transactions on Magnetics*, Vol. 53, No. 1, 1–12, Jan. 2017.

[13] Zhu, Z. Q., H. Hua, D. Wu, J. T. Shi, and Z. Z. Wu, "Comparative study of partitioned stator machines with different PM excitation stators," *IEEE Transactions on Industry Applications*, Vol. 52, No. 1, 199–208, Jan.–Feb. 2016.

[14] Zhang, Z., W. Hua, Y. Wang, X. Li, X. Zhu, and M. Cheng, "Relationship between slot-pole combination and performance of partitioned-stator field-excitation brushless machines by air-gap field modulation principle," *IEEE Transactions on Transportation Electrification*, Vol. 10, No. 4, 10 410–10 419, Dec. 2024.

[15] Jang, D. and J. Chang, "Effects of flux modulation poles on the radial magnetic forces in surface-mounted permanent-magnet vernier machines," *IEEE Transactions on Magnetics*, Vol. 53, No. 6, 1–4, Jun. 2017.

[16] Shen, Q., J. Cheng, D. Guo, and T. Yang, "Analysis and suppression of electromagnetic vibration noise of fractional-slot concentrated-windings interior PMSMs," *IEEE Transactions on*

Transportation Electrification, Vol. 10, No. 3, 5270–5281, Sep. 2024.

[17] Liu, G., R. Guan, and L. Xu, "Unequal stator modulated teeth structure to reduce electromagnetic vibration in permanent magnet vernier machine," *IEEE Transactions on Industrial Electronics*, Vol. 70, No. 12, 12 036–12 047, Dec. 2023.

[18] Elamin, M., Y. Yasa, Y. Sozer, J. Kutz, J. Tylenda, and R. L. Wright, "Effects of windows in stator and rotor poles of switched reluctance motors in reducing noise and vibration," in *2017 IEEE International Electric Machines and Drives Conference (IEMDC)*, 1–6, Miami, FL, USA, 2017.

[19] Nakata, K., K. Hiramoto, M. Sanada, S. Morimoto, and Y. Takeda, "Noise reduction for switched reluctance motor with a hole," in *Proceedings of the Power Conversion Conference-Osaka 2002 (Cat. No.02TH8579)*, Vol. 3, 971–976, Osaka, Japan, 2002.

[20] Gan, C., J. Wu, M. Shen, S. Yang, Y. Hu, and W. Cao, "Investigation of skewing effects on the vibration reduction of three-phase switched reluctance motors," *IEEE Transactions on Magnetics*, Vol. 51, No. 9, 1–9, Sep. 2015.

[21] Zhu, S., J. Ji, W. Zhao, G. Liu, and C. H. T. Lee, "Vibration reduction design of consequent pole PM machine by symmetrizing local and global magnetic field," *IEEE Transactions on Industrial Electronics*, Vol. 70, No. 1, 243–254, Jan. 2023.

[22] Zhao, W., S. Zhu, J. Ji, G. Liu, and Y. Mao, "Analysis and reduction of electromagnetic vibration in fractional-slot concentrated-windings PM machines," *IEEE Transactions on Industrial Electronics*, Vol. 69, No. 4, 3357–3367, Apr. 2022.

[23] Zhu, S., W. Zhao, Y. Shen, X. Zhu, Y. Zhou, and C. H. T. Lee, "Investigation of vibration behaviors of dual permanent magnet vernier machine considering field and force modulation effects," *IEEE Transactions on Transportation Electrification*, Vol. 11, No. 1, 2759–2769, Feb. 2025.

[24] Guan, R., Z. Liu, L. Xu, and G. Liu, "Electromagnetic vibration analysis of the permanent magnet vernier machine with dynamic eccentricity effect," *IEEE Access*, Vol. 13, 111 793–111 801, 2025.